Highlights

A Multispectral Dataset for the Detection of *Tuta absoluta* and *Leveillula taurica* in Tomato Plants

P.S. Georgantopoulos, D. Papadimitriou, C. Constantinopoulos, T. Manios, I. N. Daliakopoulos, D. Kosmopoulos

- Unique dataset of multispectral images of Tuta absoluta and Leveillula Taurica, in real greenhouse environment.
- Dataset is publicly available.
- Disease detection (localization and classification) with Faster-RCNN. Two Faster-RCNN architectures: one for RGB images and one for six-channel images (RGB, 850nm, 980nm, segmented NDVI)
- Foreground segmentation using NDVI and 630 nm, with Normalized Correlation Coefficient maximization, for non deterministic image thresholding.

A Multispectral Dataset for the Detection of *Tuta absoluta* and *Leveillula taurica* in Tomato Plants

P.S. Georgantopoulos[a], D. Papadimitriou[b], C. Constantinopoulos[a], T. Manios[b], I. N. Daliakopoulos[b], D. Kosmopoulos[a]

[a] *Computer Engineering and Informatics Dpt., University of Patras, 26504, Patras, Greece*
[b] *Dpt. of Agriculture, Hellenic Mediterranean University, 71410, Heraklion, Greece*

Abstract

Tomato (*Solanum lycopersicum*) is one of the most important vegetables for human nutrition and its cultivation employs amounts of resources worldwide. However, tomato cultivation is plagued by several diseases and pests that increase production cost and introduce additional environmental and health risks due to pesticide use. Timely disease and pest detection is of high importance for tomato crop output and the environment, since plant protection input can be optimized. Here, we present a dataset of multispectral images (RGB and NIR) of tomato plants, at various stages of infection with *Tuta absoluta* and *Leveillula taurica*, which to our knowledge is unique. The dataset comprised of 263 images collected from a real greenhouse. Additionally, we applied a baseline Faster-RCNN object detector for the localization and classification lesions. Our experiments include (i) a version for the RGB channels and (ii) a custom backbone architecture version for feature fusion using the same Faster-RCNN head. Lastly, based on the detector's output, we compute an > 0.9 F1-score on binary classification, while mAP 18.5% and mAP 20.2% on detection, highlight the added value of NIR spectral bands for detecting these diseases.

Keywords: Plant Disease Dataset, *Tuta absoluta*, *Leveillula taurica*, Leaf Miner, Powdery Mildew, Faster-RCNN, Feature fusion.

Introduction

Tomato (*Solanum lycopersicum*) is a major horticultural crop cultivated in temperate zones worldwide, with an estimated global production of over

170 million tons (Mt) [1]. The transboundary expansion of tomato demand has provided novel opportunities for the agricultural and marketing industries. However, this globalization of agricultural production has significant consequences on the globalization of agricultural pests [2]. The development of the world trade system has resulted in a sharp increase of the number of pest species invading new regions, causing reduction of vegetable crops productivity and setting product post-harvest shelf-life at risk [3]. Two such major nuisances of solanaceous crops are the tomato leaf miner *Tuta absoluta* (TA) and the powdery mildew *Leveillula taurica* (LT), also known as oidium.

TA (Meyrick) (Lepidoptera: Gelechiidae) [4] originates from S. America and is considered one of the most rapidly expanding and devastating tomato crop pests due to its high reproductive rate and damage potential, causing complete and non-refundable destruction of the crop if no proactive measures are taken [5]. The development cycle of the insect depends on the prevailing temperatures of the cultivation period. Females of TA lay up to 250 eggs on the areal part of the plant where young larvae (the worms/offsprings of the fly that feed on the leaf) start feeding from the canopy of the plant leaving characteristic irregular lesions in the form of galleries (mines) on the leaves (Fig. 1) and move to new feeding locations for as long as food is available. At the beginning of the infestation, 1st and 2nd instar larvae form small white galleries on the leaves, while in 3rd and 4th larval stages the galleries expand into new leaves and the symptoms become dark brown and necrotic. These lesions consist of dark color excrement and extensive infestation can cause complete necrosis of the leaves and defoliation. If climatic conditions are favorable, larvae feed almost continuously and generally do not enter diapause [6]. When an infestation occurs, TA larvae can cause yield losses of 50%–100% [7], therefore control at early stages is imperative.

Powdery mildew is an endoparasite forming both endophytic and epiphytic mycelium [8] initially reported in warm arid to semiarid climatic zones in Asia, the Mediterranean and Africa [9]. In tomato, powdery mildew usually infects only the mature fully developed leaves and severe infections may result in considerable damages. The main symptoms are yellow irregular spots (about 10-15 mm in diameter) on the abaxial side of the leaves (Fig. 1) and on the adaxial surface a thin light brown mycelium is formed due to the emergence of the conidiophores through the stomata [10, 8]. Several studies report yield losses of up to 40% in greenhouse and field tomatoes [11]. Desneux et al [12] report that, unless effective control measures are taken, the disease can cause yield losses of up to 80–100% in tomato crops in

recently invaded areas and may pose a threat to both greenhouse and open-field tomato production. Furthermore, disease severity on canopy of the crop can result in significant degradation of the fruit quality of canning tomatoes [10].

(a) (b)

Figure 1: (a): Tomato leaf miner 2^{nd} instar larvae feeding from mesophyll cells of tomato leaves. (b): Yellow spots on the abaxial side of tomato the leaves, at early stages of powdery mildew infection.

As the incidence of crop diseases and pests is increasing, novel, accurate and timely methods to identify early symptoms must be employed [13, 14]. Until now, the prevalent method of detecting pests and diseases heavily depends on farmer knowledge and experience, often resulting in late, inaccurate, and ineffective management of the risk. Moreover, despite the intensive research for alternative risk management methods against pest and plant diseases, the conventional method of handling the problem using chemical plant protection products is the most common strategy employed in the Mediterranean cultivational region until today [15, 16]. Unfortunately, if pathogens and pests are well established in the cultivation, pesticide and fungicide efficacy might be compromised as well as contribute to the development of resistance in a wide range of antifungal and insecticidal compounds [17, 18]. For this reason, insecticide and fungicide applications are often preventive, thus introducing an additional fixed cost that amounts to over 15% of the operating cost [19], without accounting for the associated labor, environment, and health hazard costs.

The evolution of machine learning - based vision methods (e.g., [20, 21, 22]), along with the commercial availability of RGB and multispectral vision sensors (e.g., [23], [24]) facilitate the development and deployment of automated systems for disease detection. Such systems may be used to modernize greenhouse cultivation, by reducing dependence on labour and agrochemicals. They can potentially allow the individualized management of the plants, as opposed to the current practice of indiscriminate plantation-wide interventions, which leads to resource wastage and often excessive use of agrochemicals. In addition, they can reduce the need for human presence and manual interventions, and allow for round-the-clock operation of the greenhouse.

In this context, we introduce a new publicly available dataset of multispectral images: 3 RGB and 2 Near Infra-Red (NIR) channels, of tomato plants, at various stage of infection by TA and LT. Additionally, we apply a system suited for detecting the lesions caused by TA and LT. The system framework employs a deep object detection architecture. Finally, we run a baseline model, Faster-RCNN and which has been used in the PASCAL VOC 2007 [25] (73.2% mAP) and 2012 (70.4% mAP) challenges.

Related Work

Object detection

Since lesions created by TA and LT have distinct visible characteristics, we can consider them as objects which can be located on an image. In the literature, this problem is called object detection and has been studied extensively. As described by Wand et al. [26], salient object detection in the Deep Neural Network (DNN) era starts from Multi Linea Perceptron (MLP) - based architectures, until recent works, using Fully Convolutional Neural Networks (FCN).

State of the art frameworks use Region-based CNNs (RCNNs), which incorporate a Region Proposal Network (RPN), while allowing scale invariant detections by using Feature Pyramid Networks (FPNs).

A basic setup of an object detector is comprised of a feature extraction module - in the case of a deep architecture this is a classic deep architecture like ResNet [27] or VGG [28] that have been proven efficient without the pre-application of any other heuristic rules. These features are used next by other modules for tasks like classification, segmentation or salient map generation, according to the application.

One of the most prominent FCN frameworks is Faster-RCNN [29]: a two-stage object detector using an RPN with data driven anchors and a *"head"* module responsible for fine tuning and classifying Region of Interest (RoI) proposals. The use of the RPN escapes the time consuming process of Selective Search [30] used in preceding works like RCNN [31] and Fast-RCNN [32]. The main difference can be found at testing time, where a CNN feedforward procedure is less laborious than the process of forming homogeneous regions with Selective Search.

R-FCN [33] is in principal the same as Faster-RCNN with the only difference that it has score maps to evaluate the proposed RoIs. SSD [34] is a single stage object detector which uses multiple convolutional layers for multiple scales scales. The same holds for the Yolo framework, for which multiple models have been published: Yolo9000 [35], Yolov3 [36] and Yolov4 [37], focusing or real time object detection. Another single-stage detector, RetinaNet 2018 [38], is similar in structure to Faster-RCNN, but feature maps are produced by Nearest Neighbors sampling, rather than using an RPN. Lastly, CornerNet [39] and RepPoints [40] try a different representation for ground truth regions, using points instead of bounding boxes. Also, FCOS [41] propose a one-stage fully convolutional detector which avoids the use of an RPN. DeNet [42] also uses corners to base its RoI proposals.

Deep learning for the detection of plant diseases and pests

Recent research studies propose novel detection methods based on deep neural networks and object detection models to tackle the challenge of early detection of the plant pest and disease symptoms [43]. Raza et al. [44] have demonstrated data collection through Electronic Nose (EN) coupled with NN techniques for analysis and classification of infected (powdery mildew) and healthy tomato crops with a maximum of 98% accuracy. Moreover, Xu et al. [45] investigated the application of NIR Spectroscopy by exploiting the leaf reflectance properties for detection of the leaf miner pest on tomato leaves and analyzed reflectance at different wavelengths that could differentiate infection stages. The wavelengths with maximum correlation coefficient were found to be 1450 nm and 1900 nm. Recently, the research project "SOUP: SOilless culture Upgrade" aims to automate the monitoring of plant growth through sensor networks, and to introduce robotic technology for pest management [46].

Works like [47], [48], [49], [50] and [51] target specifically tomato plants, providing a dataset on *Tuta absoluta* under green house conditions. They

compare pretrained fully convolutional networks to identify the disease present in the image. The major difference with our dataset is that the labeling is done upon the whole image and not on the RoI, resulting in a classification, rather than a detection task. Also each image frames a single leaf at a time, usually with the leaf facing the camera. In our case, where the whole plant is framed, leaves can be facing in all directions, changing the patter of the lesion altogether. This makes the detection task a more complex problem for the detector to solve.

On the other hand, [52] aim to the localization of the disease in the image. However, the dataset they use is inconsistent in resolution, coming from heterogeneous sources, which may account for different spectral response as well. However, the content of each image is mostly a single leaf. Also, the annotation they provide is limited to a bounding box, while we provide bitmap masks which can be used for a more vast range of architectures, such as Mask-RCNN [53].

To add to our contributions, all of the above datasets are in the visible spectrum, while our dataset includes not only two infrared channels but also three channels in the visible spectrum of a more narrow band response. Xu et al [54] use a similar setup with far-infrared spectral bands ($7\mu m \sim 12\mu m$ and), but the installation they use for acquiring the images provides only a top view of the image.

From the above we infer that the attention on plant disease detection using Deep Learning is evident in literature. The reader is referred to the survey papers of [55] and [56] for more such works.

Datasets of plant diseases and pests

In literature there is a variety of works studying the detection of plant diseases in images. Plenty of them employ DNN architectures to achieve efficient disease detection, while others introduce new datasets to enable further research on the topic. Attributes of relevant datasets are the plants under consideration, the diseases, the captured spectra, the content of the images and the environment in which it is acquired. To keep things in perspective to our contribution, some of the dataset also consider the tomato plant, while a few use multispectral imaging to detect a disease. For example, works like [57, 47, 49, 52, 58, 54, 59] include cases of diseased tomato plants in their datasets. At the same time, [60, 52, 58, 51] and [59] include TA and LT on tomato plants, alongside other plant diseases. Furthermore, [61, 62, 63, 64, 65, 66, 67] and [54] use multispectral (MS), hyperspectral (HS)

or NIR imaging in the datasets they use. However, NIR may be included in MS or HS bands. Lastly, only three datasets are publicly available: Plant Village/Plant Disease [51, 50], Early Crop Weed [48] and Plant Pathology Apple [65].

A summary of the related datasets and their features are given in Table 1. It is evident that a public dataset in real greenhouse environment including NIR channels is missing. Even more so there is no multispectral data in this context for TA and LT, at all.

Table 1: Datasets and relevant works in literature. Tomato plants, *Tuta absoluta*, *Leveillula taurica* and NIR occurrences are in bold. S: spectra, D: dataset (u: undisclosed, p: public), F: framing (l: leaf, p: plant), E: environment (l: lab, f: field, g: greenhouse).

Ref.	Plant:Disease or pest	S	D	F	E
[57]	**tomato**: no disease reference	RGB	u	p	f
[60]	**tomato**: **Leaf miner** et al.	RGB	p	p	f
[47]	**tomato**: **Tuta absoluta**	RGB	u	p	f
[48]	tomato, cotton: Black nightshade, Velvet leaf	RGB	p	p	f
[49]	**tomato**: Early Blight, Late Blight, Citrinitas leaf curl, Leaf mold, Bacterial leaf spot	RGB	p	p,l	l
[52]	**tomato**: Leaf mold, Gray mold, Canker, Plague, **Miner**, **Powdery mildew**, Whitefly, Nutritional excess	RGB	u	p	f
[68]	unspecified: **Powdery mildew**	RGB	u	p	f
[58]	**tomato**: **Powdery mildew**, spotted wild virus	RGB	u	p	l
[51, 69, 70, 71]	Cherry: **Powdery Mildew**; Squash: Healthy, **Powdery Mildew**; **tomato**: Bacterial Spot, etc	RGB	p	l	l
[54]	**tomato**: Tobacco mosaic virus	**NIR** (7-1μm,8-14μm)	u	p	l
[50]	**tomato**: Bacterial spot, etc	RGB	p	l	l
[67]	wheat: **Powdery mildew** etc	HS (17 bands in [445nm, 870nm])	u	p	l
[72]	common bean: **Powdery mildew**; coffee:**Leaf miner**, etc; cashew tree: **Powdery mildew**; kale: **Powdery mildew**, etc	RGB	p	l	l
[66]	unspecified: Theba pisana insect	RGB, UV, **NIR** (700-1500nm)	u	p	
[65]	apple: Rust, Scab	HS(1.6-5.9μm)	p	p	l
[64]	cassava: Brown streak	MS (15 bands in [395nm, 880nm])	p	l	l
[63]	cucumber:**Powdery mildew**	MS (430-470nm, 630-690nm)	u	l	l
[62]	wheat: Crown rot	HS(450-497nm)	p	p	l
[73]	sugar beet: Leaf spot	RGB	u	p	f
[74]	rice: Stackburn, Leaf smut, Leaf scald, White tip, Leaf streak; Maize: Phaeosphaeria spot, Eyespot, Gray leaf spot, Goss's bacterial wilt	RGB	p	l	l
[61]	cucumber:**Powdery mildew**	MS (475, 560, 668, 840, 717nm)	p	p	g
[59]	**tomato**: Early blight, Late blight, Gray leaf spot, Brown spot, Coal pollution, Gray mold, Leaf mold, Powdery mildew, Leaf curl, Mosaic, **Leaf miner**, Greenhouse whitefly	RGB	p	p	f

Dataset development

Greenhouse setup

Tomato seedlings (*Solanum lycopersicum* var. Elpida) at the stage of four true leaves were transplanted in rockwool slabs in an unheated saddle roof

double-span greenhouse covered with polyethylene film, at the experimental greenhouse facilities of the Hellenic Mediterranean University, Greece. To avoid translocation of the pest and fungal disease, plants were grown in separate insect-proof chambers (12 m^2) designed to accommodate six fully developed tomato plants. To produce an artificial leaf miner infestation, a *T. absoluta* colony was initiated from insects collected in from a local commercial greenhouse and maintained for four weeks in the laboratory (Temperature 25 °C; Relative humidity 75±5%; 12 h Light : 12 h Dark) by feeding on tomato plants (*Solanum lycopersicum* var. Elpida). After eight weeks, adult insects were transferred in two insect-proof chambers of the experimental greenhouse and infection-free tomato plants (n=12) at the stage of nine fully developed leaves were colonized with adult insects (3 adults m^{-2}).

To produce an artificial powdery mildew infection, *Leveillula taurica* (Ery siphaceae) was isolated from young leaves of tomato plants grown in a local commercial greenhouse. Conidia, i.e., the spores of the fungus were collected by intensively washing infected leaves with water. The conidia in the rinse suspension were counted under a light microscope using a hemocytometer. For inoculations of tomato leaves, the concentration of conidia in the suspension was adjusted to 2 104 conidia ml^{-1}. The suspension was sprayed onto tomato plants (n=12) at the stage of nine true leaves unfolded at a volume of 5 ml per plant [75]. Inoculated plants were kept in growth chambers for 24 h in plastic cages with 100% relative humidity at 21 °C. Consecutively, the tomato pants were transferred in two separate insect-proof chambers in the experimental greenhouse. After treatment, tomato plants were fertigated daily with a standard nutrient solution calculated after [76] using an IQ60 automatic nutrient mixing system (Alagro, Greece).

Image acquisition

Two weeks after the artificial (*L. taurica*) inoculation and (*T. absoluta*) colonization, multispectral images of the tomato plants were captured every three days. In this study we used the MUSES9-MS-PL multispectral camera (Spectricon, Greece), which features 4-6 Megapixels C-MOS @ 25 f/s in the 370-1100 nm spectral range. The camera implementation used here captures a total of 8 channels per shutter click at a resolution of 1776 by 2368 pixels. The first 3 channels are acquired with a typical RGB sensor while the rest are captured via the multi-spectral sensor. Three of the latter channels were chosen to be at 460 nm (near blue), 540 nm (near green), and 630 nm (near red), respectively. These wavelengths are typically close to the ones used in

the RGB camera, however the response of the multi-spectral sensor is denser around these frequencies than the response of the RGB camera. The last 2 channels are in the Infra-Red spectral region, at 850 nm and 980 nm. Table 3 shows the width of each band. MUSES9 applications include non destructive object analysis [77], biomedical optical imaging [78], pigment identification and mapping in paintings [79], and multispectral microscopy of micro-plastic pollution [24].

The dataset contains at total of 314 images, labeled by plant, date, symptom and RoI. Within the dataset 179 images show TA symptoms, 103 show LT symptoms, and 32 show no symptoms Table 2. Since plants were captured at different development stages, therefore the images depict both the early and late stages of pest or disease symptoms. In addition, the dataset is acquired with a total of 5 channels: 460 nm, 540 nm, 630 nm, 850 nm, 980 nm, in comparison to most datasets in the bibliography were acquired solely with standard RGB cameras. Finally, since images were taken from within the experimental greenhouse, consistent and realistic environmental conditions are kept throughout the dataset. Image calibration was not performed under the assumption that a LED light source provided consistent illumination throughout the dataset. The light source was installed around the camera lens and the images were taken during the day. The light source is a circular array of led bulbs emitting in ultraviolet (UV), visible and NIR spectra. Coarsely, there is a monotropic narrow response in UV with a mode at $\sim 375nm$, a wider response in the visible spectrum with a mode at $\sim 550nm$ and an also wide response in NIR with a mode at $\sim 900nm$. The dataset is openly accessible for future development[1]. A sample cube can be found in Figure 2.

Image annotation

Each image was manually annotated by an expert agronomist using the VGG Image Annotator tool [80]. Each lesion was localized with a bounding box, and the results were stored in JSON files using the format proposed for the COCO object detection dataset[2]. As secondary metadata of the dataset, each lesion was also labelled based on its level of progression, with 1 denoting 1-5 lesions, 2 denoting to 5-10 lesions, and 3 denoting 10-20 lesions. In cases

[1] `https://drive.google.com/drive/folders/1gzhT03EY5WxxYJT0k8EAsBiahc9lVG-S?usp=sharing`

[2] https://cocodataset.org/#format-data

Table 2: Number of samples per lesion type and progression level in the dataset.

Disease progression level	TA samples	LT samples
0	32	0
1	122	97
2	30	6
3	27	0
Total	211	103

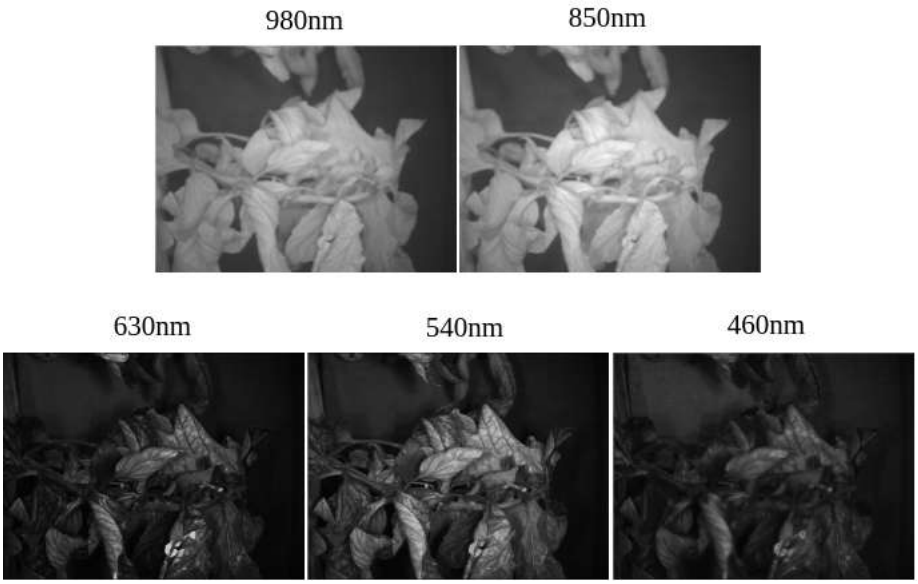

Figure 2: A multispectral cube of the dataset. *top*: the NIR channels at 850 nm and 980 nm. *bottom*: channels of the visible spectrum in the wavelength regions of red, green and blue (see Table 3).

Table 3: Wavelength regions supported by the MUSES9-MS-PL camera and those used in the current study.

Spectral band	Lower limit (nm)	Upper limit (nm)	Current study (nm)	FWHM* (nm)
Infrared	800	1000	980, 850	50
Red	600	700	630	40
Green	500	600	540	30
Blue	400	500	460	30
Ultraviolet	365	385	-	-

* FWHM: Full Width at Half Maximum

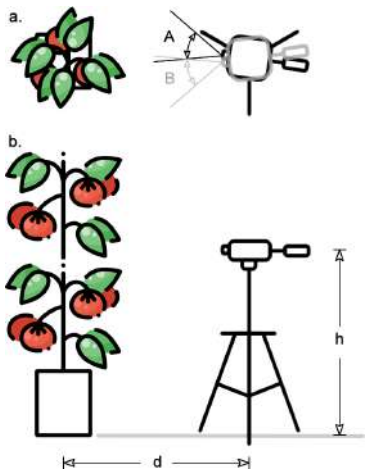

Figure 3: Top view (a) and side view of (b) the multispectral image sampling arrangement. The camera is set at distance d = 1.00 m from the tomato plant. Images were acquired from three heights (h = 0.75, 1.00, 1.40 m) and two azimuth angles (A = 15°and B = -15°).

of higher progression, the pest and disease symptoms has surpassed a critical point where lesion detection, for the purpose of prevention, would have no interest. Images with no visible symptoms were annotated as level 0.

Automated detection methods

Foreground segmentation

To calculate the Lesion to Healthy Ratio (LHR), we had to segment the foreground of the image, that consists of green plant biomass. To do so, we applied a histogram-based thresholding on the NDVI image. The optimal threshold was selected according to the green channel (540 mn) and the NDVI image. The Normalized Difference Vegetation Index (NDVI) is vastly used in the literature [81, 82] for the distinction of yield-related physiological traits [83], and it is computed as follows:

$$I_{NDVI} = \frac{I_{NIR} - I_{Red}}{I_{NIR} + I_{Red}}$$

where NIR is channel 980 nm and red is channel 630 nm. The threshold used is not selected arbitrarily, rather it is computed as the argument that maximized the Normalized Correlation Coefficient (NCC) between channel

540 nm (I_{540}) and NDVI (I_{NDVI}). The NCC between these two images is defined as the following scalar quantity:

$$NCC(I_{540}, I_{NDVI}) = \sum_{i,j=1}^{H,W} \left[\frac{(I_{540} - \hat{I}_{540}) \circ (I_{NDVI} - \hat{I}_{NDVI}))}{\sigma_{540} \times \sigma_{NDVI}} \right]_{[i,j]}$$

where the $\circ$ operator is the element-wise Hadamard product, H and W are the height and width of the images. I_{540} and I_{NDVI} are the thresholded channel 540 nm and NDVI respective images given a set of thresholds aiming to isolate the supports of the useful lobes of their histograms. $\hat{I_{540}}$ and $\hat{I_{NDVI}}$ are the mean pixel intensities of the above images. The process is repeated systematically over various sets of thresholds. The pair yielding the highest NCC is kept.

The idea behind this procedure is that NDVI alone cannot be systematically thresholded with no regularizer being present. This is the point of introducing channel 540 nm here, to act as a regularizer, since in an ideal scenario it contains the greener parts of the image, most likely leaves. Lastly, what we refer to as "threshold" is actually a tuple of intensities, meaning that the histogram was cropped in order to match exactly the lobe of the histogram corresponding to the leaves. A segmentation example can be seen in Figure 4.

The advent of accessible multispectral cameras allowed the use of NDVI at lab scale, with recent applications in tomato canopy [84, 85] and health assessments [86, 87, 88]. Nevertheless, to our knowledge, NDVI has not been implemented within a machine learning framework for pest or disease detection.

(a) RGB image (b) NDVI image (c) Segmented image

Figure 4: NDVI image computed from the 630 nm and 980 nm channels, *bottom*: Segmented image.

Faster-RCNN and its Multichannel Variant

A state of the art model for object detection is Faster-RCNN [29]. The outputs of RPN are evaluated towards their probability of containing an object or not, with the use of a convolutional layer. What boxes are likely to contain an object are passed though a Non-Maximal Suppression module, which discards boxes that have an overwhelming overlap, except one. The remaining bounding boxes are classified with an other convolutional layer, producing final predictions of bounding boxes along with their classes. During training, the RPN is trained separately from the rest of the network. Namely, proposals are regressed towards the ground truth boxes. For details on this procedure we suggest referring to the work of [32].

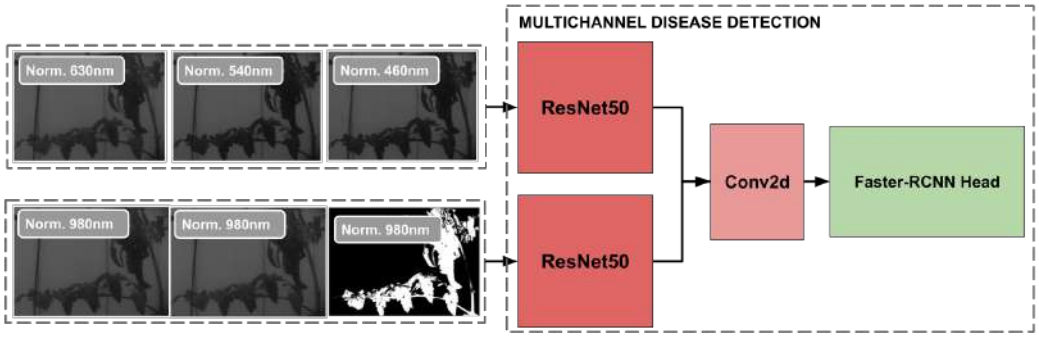

Figure 5: Design of the Multichannel Disease Detection Module. It can replace the Disease Detection part of the pipeline to in order to use more than 3 channels.

When it comes to utilizing the full set of bands available we used a custom model with Faster-RCNN head and the two identical pretrained backbones: one for the RGB channels and one for the 850 nm. This idea is similar in principal to [89]. In more detail, as shown to Figure 5,the features produced by two ResNet architectures are merged together using a simple 2d convolutional layer and fed into the Faster-RCNN head.

Performance measures

A straightforward method to evaluate an object detector is to compute the Intersection over Unions (IoU) between the output boxes and the ground truth boxes. Figure 6 illustrates the IoU. However this naive approach omits entirely what makes a good detector, which is the precise prediction of the ground truth box with a single detection. For example, a detector that

achieves a high IoU predicting multiple bounding boxes per ground truth box, is not considered to be a good one. The questions arising how to treat duplicate detections. The answer depends on the decision rule applied. That filtering step can be based either on IoU, classification scores of a mix of those two. What COCO algorithm does is it integrates over an IoU curve. Keeping a low IoU threshold between prediction and ground truth will allow smaller predictions to pass through, while a higher threshold will accept only a high overlap between the two. In detail, COCO thresholds duplicate detections solely on IoU and does so for multiple threshold values, ultimately computing an Average Precision. Doing so for all classes yields a mean Average Precision (mAP). For reference, we used the Pycocotools [3] implementation library. In their implementation each ground truth box matches the best prediction (score-wise and the IoU-wise). Mean AP has become a benchmark metric in the latest object detection literature and in competitions like LSVRC and COCO.

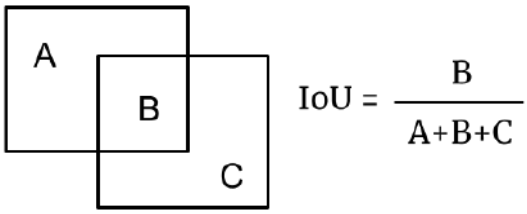

Figure 6: Intersection over union (IoU) between to closed curves, here two bounding boxes. A and C are the areas of the non-intersected sections and B is the intersection. The some of all defines the union area.

Apart from the COCO metrics, what we think will prove valuable from the agronomist's perspective is to evaluate our results in a different manner. For that reason we also evaluated each image as a single detection. In detail, if a single detection is matched to a ground truth box, the image is considered as a True Positive (TP). If there are no detections but there is at least one ground truth box, the image counts as False Negative (FN). In the contrary, if there is at least one detection but no ground truth boxes, it counts as a False Positive (FP).

[3]https://github.com/cocodataset/cocoapi/tree/master/PythonAPI/pycocotools

Deep Learning design

The proposed modules of the pipeline are shown in Figure 7. After image acquisition (see b), the spectral cube is normalized over mean and standard deviation, in order to follow the priors introduced by the dataset COCO, in [90], which we used for pre-training our models. Moving on at the third step, these cubes are fed to the detection pipeline of a deep neural network, which produces bounding boxes of the form $(x, y, width, height)$, and their respective classification scores. Each bounding box defines the limits of a prospective lesions. At the final step, the resulting bounding boxes are filtered based on the confidence of the network. The remaining detections are used to calculate two indices. The first is for performance evaluation, namely we calculate the Average Precision (AP), as proposed in the COCO evaluation procedure [90]. The second one is the ratio of lesion area to healthy leaf area (see section b), which is a useful measurement for the agronomist, as an estimation of the stage of the disease.

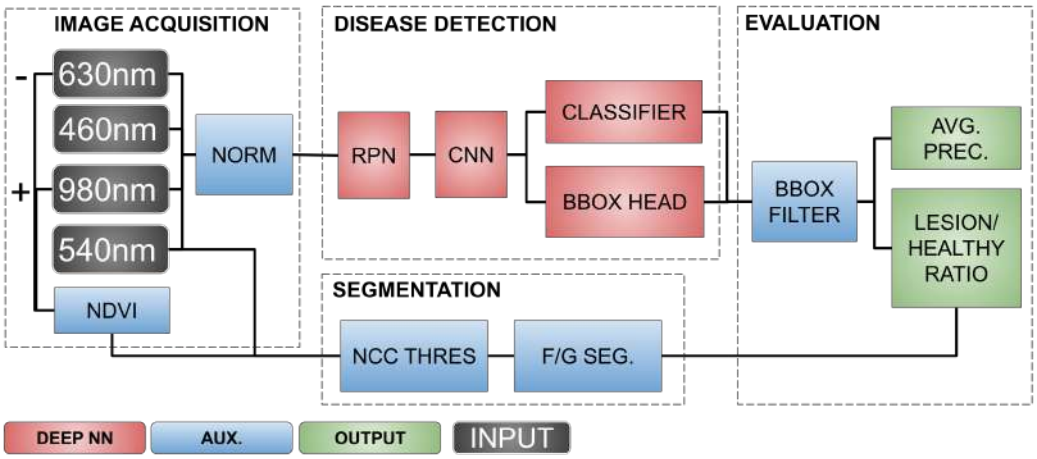

Figure 7: Design of the Deep Learning pipeline.

Experimental Design and Evaluation

In our experiments we aim to showcase the feasibility of using a deep learning lesion segmentation framework in real conditions and and the potential to use NIR the channel to improve its efficiency.

The main tool we used was the Pytorch Faster-RCNN[4] implementation with a ResNet50 backbone feature extractor pretrained on ImageNet [91], while the whole network was pretrained on COCO '17. From this snapshot of the model we continued training using the *"approximate joint training method"*; that is the losses from the classifier, bbox regressor and RPN-bbox regressor were added together to form a loss which is back-propagated throughout the model parameters. Finally, we selected IoU and classification score thresholds for our own evaluation method, while for the COCO evaluation we left it at its default values (IoU threshold = 0.5 and score threshold = 0.5).

To clearly showcase the added value of the NIR channels, we set up two experiments. In the first experiment, dubbed A, we used channels 630 nm, 540 nm, 460 nm as a three channel input to a vanilla pretrained Faster-RCNN model.

In the second experiment, B, we improvised a two parallel backbone architecture to add three more channels to our input. Those channels were 850 nm, 980 nm and thresholded NDVI. The third one is basically a mask for the leaf area of the cube. In this experiment achieved a higher mAP score (see Table 4).

To elaborate a bit on the results we need to clarify some notions of the COCO evaluation. When matching ground truth boxes to detections, COCO considers a maximum number of detections, *maxdets* beyond which all detections are discarded. This threshold is set by default at values 1, 10 and 100. *bbox_sizes* represents what types of boxes are used for evaluation. Detections are divided into small, medium and large based on their size. What this manages to show is how the system performs in those cases separately.

Figure 4 gathers the two experiments in its two three columns. We achieved mAP values of 16.0% and 20.2% for A and B, respectively; this may appear low, but one should keep in mind the operational conditions of an actual greenhouse, rather than a laboratory, under which the images were captured. Our speculation is that the variety in ground truth bounding boxes sizes and aspect ratios, in combination with the uneven distribution of occurrences across images, yielded a low mAP value due to averaging out, which is agnostic to such kind of parameters.

Finally, results for the second performance measure technique, discussed

[4]https://pytorch.org/vision/0.8/models.html#faster-r-cnn

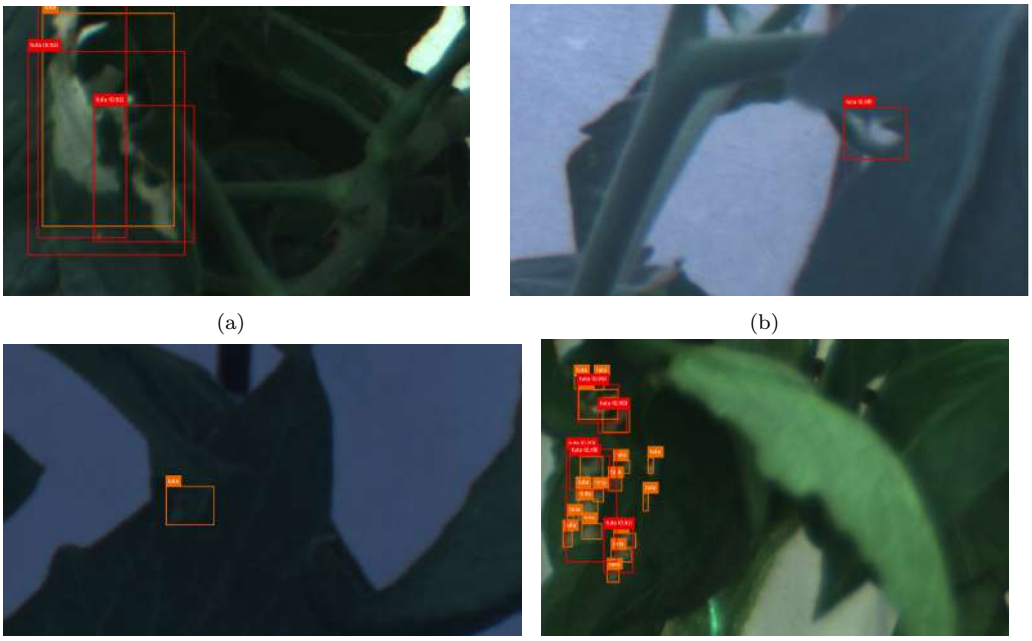

(a) (b) (c) (d)

Figure 8: (a): False positives due to multiple detections for a single ground truth and (b): with an ambiguous ground truth due to low visibility. (c): False negative example due to low visibility and (d): due to a "crowd"-like group of lesions.

Table 4: Evaluation results of Faster-RCNN detector using the Pycocotools library. Mean average precision appears in bold. The two tables refer to experiments A and B, respectively. For each metric, the score for each output class is also provided. Results are averaged over a five-fold cross validation.

Metric	IoU	bbox sizes	max.dets	Exp. A	TA presence	LT presence
AP(**mAP**)	0.50:0.95	all	100	**0.187**	**0.083**	**0.296**
AP	0.50	all	100	0.475	0.253	0.717
AP	0.75	all	100	0.084	0.022	0.174
AR	0.50:0.95	all	1	0.117	0.04	0.2
AR	0.50:0.95	all	10	0.258	0.135	0.379
AR	0.50:0.95	all	100	0.266	0.147	0.379

Metric	IoU	bbox sizes	max.dets	Exp. B	TA presence	LT presence
AP(**mAP**)	0.50:0.95	all	100	**0.196**	**0.099**	**0.303**
AP	0.50	all	100	0.506	0.278	0.755
AP	0.75	all	100	0.094	0.038	0.147
AR	0.50:0.95	all	1	0.121	0.045	0.201
AR	0.50:0.95	all	10	0.264	0.146	0.39
AR	0.50:0.95	all	100	0.276	0.165	0.39

in section b, are shown in Table 5. Again, the addition of extra channels as input to our model, along with the second backbone that is used, evidently improve results. The purpose of this evaluation technique is to answer to the expert's question "Is there presence of lesions on this plant?". This question's easiness to answer using an object detector is projected on the numerically high ($> 90\%$) results it yields.

It is also evident from the results that the model performs better overall

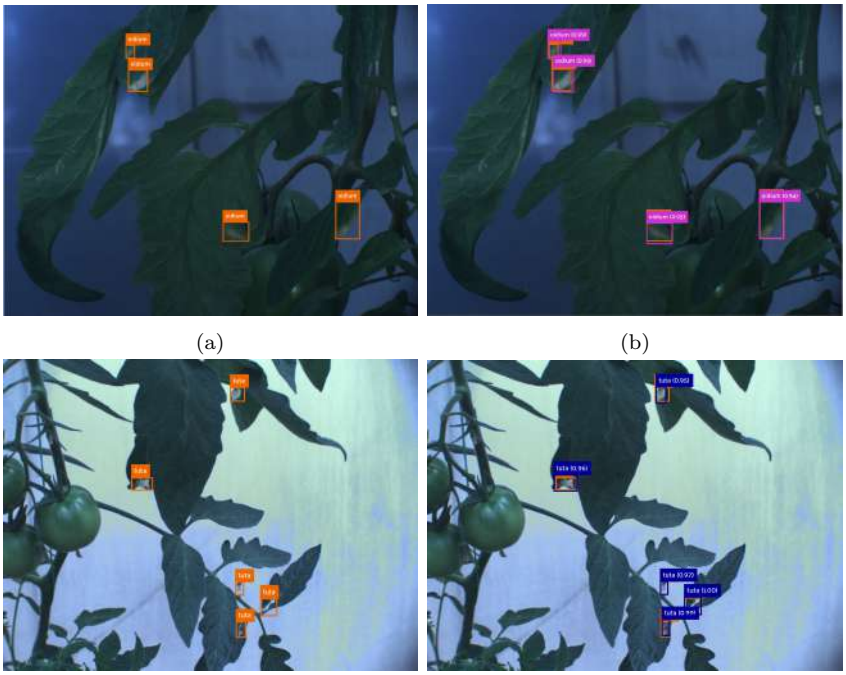

(a) (b)

(c) (d)

Figure 9: Detection results using Faster-RCNN for (a,b): *Leveillula taurica* and (c,d): *Tuta absoluta*

for LT for either metric. That could be due to LT having a subtle appearance on the leaf, with approximately constant aspect ratio. In the contrary TA is clearer to the eye, grows and changes shapes in a faster pace. Thus, it is speculated that the consistency in LT examples makes its detection an easier problem than the detection of TA.

Table 5: Detection results using the proposed evaluation method. Each image constitutes a detection, which is meaningful from the agronomists perspective, since the sole presence of the disease on a plant is enough knowledge for the expert to take action. The two tables refer to experiments A and B, respectively. For each metric, the score for each class separately is also provided. Results are averaged over a five-fold cross validation.)

Metric	Exp. A	TA presence	LT presence
Precision	0.886	0.779	0.973
Recall	0.958	0.916	1.0
F1	0.92	0.854	0.986
Metric	Exp. B	TA presence	LT presence
Precision	0.857	0.724	0.99
Recall	0.957	0.914	1.0
F1	0.904	0.813	0.995

Discussion and Conclusions

To interpret our results further, we need to consider the types of false detections assessed by the proposed methods. On the one hand, false positive (FP) cases typically occur where the model interprets leaf morphology (e.g. a hole) as a lesion or when multiple detections account for a single ground truth in its neighborhood. Examples of these two cases are shown in Figure 8a. Based on the results of mAP which is affected by FPs, the use of the FPN module in the Faster-RCNN architecture helped overcome the problem of the detection of small lesions, which occur especially in the early stages of inoculation. On the other hand, false negatives (FN), which affect the mAR metric, can arise under two main scenarios. One case is when, due to low visibility (Figure 8c), it is challenging even for the expert to decide on lesion presence or absence. Another case is when a single detection accounts for multiple neighboring ground truth boxes (see Figure 8c, right). The COCO dataset format supports such an annotation attribute for a bounding box, called "crowd". However, the typical case of use is when there is an overlap of object of the same class in the image. In our case, even if there are examples of lesions extremely close together, the limit after which they should be referred to as "crowd" is unclear. This is due to the nature of the disease, which expands maze-like patterns.

The use of the latter architecture for fewer secondary channels, required an extra module to convert the number of channels to three for them to feed to the backbone. That K-to-Three channels convolutional layer introduces the problem of how to train the additional untrained modules alongside the already pretrained backbone. That is even if NIR provides additional input which can lead to better results. We tried naively training it along with the rest of the pretrained backbone, however it yielded lower results than expected which is why we set it aside for a future work.

To conclude, this work contributes a publicly available multispectral dataset on *Tuta absoluta* and *Leveillula taurica*, and presents a baseline experimentation for their localization and classification at their early stage of inoculation. This dataset is unique to our knowledge. Moreover, we have showcased that the NIR channels of the multispectral data provide added value for background extraction during preprocessing by using NDVI - 630 nm channel pairs, and can further enhance the detection results by incorporating as additional channel on top of the typically used RGB channels. The resulting dataset and methods can be readily applied in image recognition applications for greenhouse tomato cultivation, for the purpose of disease and pet management. Especially in the case of systems that support automated image acquisition such as robotic and camera rig applications.

Statements and Declarations

The authors would like to declare no conflict of interest.

Acknowledgments

This work was co-financed by the European Union and Greek national funds through the Operational Program Competitiveness, Entrepreneurship and Innovation, under the call RESEARCH - CREATE - INNOVATE (project SOilless culture UPgrade - SOUP code:T1EDK-04171). Part of the graphics adapted with Pixelmeetup www.flaticon.com.

References

[1] J. Costa, E. Heuvelink, et al., Introduction: The tomato crop and industry, Crop Production Science in Horticulture 13 (2005) 1.

[2] L. H. Ziska, D. M. Blumenthal, G. B. Runion, E. R. Hunt, H. Diaz-Soltero, Invasive species and climate change: An agronomic perspective, Climatic Change 105 (1) (2011) 13–42. doi:10.1007/s10584-010-9879-5.

[3] L. J. Olson, The economics of terrestrial invasive species: A review of the literature, Agricultural and Resource Economics Review 35 (1) (2006) 178–194. doi:10.1017/S1068280500010145.

[4] T. Kiliç, First record of Tuta absoluta in Turkey, Phytoparasitica 38 (3) (2010) 243–244. doi:10.1007/s12600-010-0095-7.

[5] G. Tropea Garzia, G. Siscaro, A. Biondi, L. Zappalà, Tuta absoluta, a South American pest of tomato now in the EPPO region: Biology, distribution and damage, EPPO Bulletin 42 (2) (2012) 205–210. doi:10.1111/epp.2556.

[6] E. Roditakis, D. Papachristos, N. E. Roditakis, Current status of the tomato leafminer Tuta absoluta in Greece, EPPO Bulletin 40 (1) (2010) 163–166. doi:10.1111/j.1365-2338.2009.02367.x.

[7] S. Ghaderi, Y. Fathipour, S. Asgari, G. V. Reddy, Economic injury level and crop loss assessment for Tuta absoluta (Lepidoptera: Gelechiidae) on different tomato cultivars, Journal of Applied Entomology 143 (5) (2019) 493–507. doi:10.1111/jen.12628.

[8] J. C. Correll, Host Range, Specificity, and Biometrical Measurements of Leveillula taurica in California (1987). doi:10.1094/pd-71-0248.

[9] A. Lebeda, B. Mieslerová, T. Jankovics, L. Kiss, E. J. Van der Linde, First detection of tomato powdery mildew caused by Oidium neolycopersici in South Africa, South African Journal of Botany 99 (2015) 153–157. doi:10.1016/j.sajb.2015.03.196.

[10] B. J. Aegerter, E. M. Miyao, T. A. Turini, C. S. Stoddard, M. Le Strange, Impact of powdery mildew (Leveillula taurica) on yield and fruit quality of processing tomatoes in California, Acta Horticulturae 1081 (2015) 153–158. doi:10.17660/ActaHortic.2015.1081.17.

[11] R. A. Guzman-Plazola, R. M. Davis, J. J. Marois, Effects of relative humidity and high temperature on spore germination and development

of tomato powdery mildew (Leveillula taurica), Crop Protection 22 (10) (2003) 1157–1168. doi:10.1016/S0261-2194(03)00157-1.

[12] N. Desneux, E. Wajnberg, K. A. Wyckhuys, G. Burgio, S. Arpaia, C. A. Narváez-Vasquez, J. González-Cabrera, D. C. Ruescas, E. Tabone, J. Frandon, et al., Biological invasion of european tomato crops by tuta absoluta: ecology, geographic expansion and prospects for biological control, Journal of pest science 83 (3) (2010) 197–215.

[13] V. López-Morales, O. López-Ortega, J. Ramos-Fernandez, L. Munoz, Japiest: An integral intelligent system for the diagnosis and control of tomatoes diseases and pests in hydroponic greenhouses, Expert systems with applications 35 (4) (2008) 1506–1512.

[14] Z. Li, Y. Li, Y. Yang, R. Guo, J. Yang, J. Yue, Y. Wang, A high-precision detection method of hydroponic lettuce seedlings status based on improved faster rcnn, Computers and Electronics in Agriculture 182 (2021) 106054.

[15] M. Brand, Y. Messika, Y. Elad, D. R. David, A. Sztejnberg, Spray treatments combined with climate modification for the management of leveillula taurica in sweet pepper, European journal of plant pathology 124 (2) (2009) 309–329.

[16] Y. Yanar, D. Yanar, N. Gebologlu, Control of powdery mildew (leveillula taurica) on tomato by foliar sprays of liquid potassium silicate (k2sio3), African Journal of Biotechnology 10 (16) (2011) 3121–3123.

[17] N. J. Hawkins, C. Bass, A. Dixon, P. Neve, The evolutionary origins of pesticide resistance, Biological Reviews 94 (1) (2019) 135–155.

[18] J. A. Lucas, N. J. Hawkins, B. A. Fraaije, The evolution of fungicide resistance, Advances in applied microbiology 90 (2015) 29–92.

[19] W. T. Kelley, G. E. Boyhan, K. A. Harrison, P. E. Sumner, D. B. Langston, A. N. Sparks, S. Culpepper, W. C. Hurst, E. G. Fonsah, Commercial tomato production handbook, University of Georgia, 2010.

[20] T. Li, Y. Ma, T. Endoh, A systematic study of tiny YOLO3 inference: Toward compact brainware processor with less memory and logic gate, IEEE Access 8 (2020) 142931–142955.

[21] Y. Koo, S. Kim, Y.-g. Ha, Opencl-darknet: implementation and optimization of opencl-based deep learning object detection framework, World Wide Web (2020) 1–21.

[22] E. Bisong, Google colaboratory, in: Building Machine Learning and Deep Learning Models on Google Cloud Platform, Springer, 2019, pp. 59–64.

[23] L. Keselman, J. Iselin Woodfill, A. Grunnet-Jepsen, A. Bhowmik, Intel realsense stereoscopic depth cameras, in: Proc. IEEE Conf. on Computer Vision and Pattern Recognition Workshops, 2017, pp. 1–10.

[24] C. M. Gwinnett, A. O. Osborne, A. R. Jackson, The application of tape lifting for microplastic pollution monitoring, Environmental Advances (2021) 100066.

[25] M. Everingham, S. A. Eslami, L. Van Gool, C. K. Williams, J. Winn, A. Zisserman, The pascal visual object classes challenge: A retrospective, International journal of computer vision 111 (1) (2015) 98–136.

[26] W. Wang, Q. Lai, H. Fu, J. Shen, H. Ling, R. Yang, Salient object detection in the deep learning era: An in-depth survey, IEEE Transactions on Pattern Analysis and Machine Intelligence (2021).

[27] K. He, X. Zhang, S. Ren, J. Sun, Deep residual learning for image recognition, in: Proceedings of the IEEE conference on computer vision and pattern recognition, 2016, pp. 770–778.

[28] K. Simonyan, A. Zisserman, Very deep convolutional networks for large-scale image recognition, arXiv preprint arXiv:1409.1556 (2014).

[29] S. Ren, K. He, R. Girshick, J. Sun, Faster R-CNN: Towards real-time object detection with region proposal networks, IEEE transactions on pattern analysis and machine intelligence 39 (6) (2016) 1137–1149.

[30] J. R. Uijlings, K. E. Van De Sande, T. Gevers, A. W. Smeulders, Selective search for object recognition, International journal of computer vision 104 (2) (2013) 154–171.

[31] R. Girshick, J. Donahue, T. Darrell, J. Malik, Rich feature hierarchies for accurate object detection and semantic segmentation, in: Proceedings of

the IEEE conference on computer vision and pattern recognition, 2014, pp. 580–587.

[32] R. Girshick, Fast r-cnn, in: Proceedings of the IEEE international conference on computer vision, 2015, pp. 1440–1448.

[33] J. Dai, Y. Li, K. He, J. Sun, R-fcn: Object detection via region-based fully convolutional networks, arXiv preprint arXiv:1605.06409 (2016).

[34] W. Liu, D. Anguelov, D. Erhan, C. Szegedy, S. Reed, C.-Y. Fu, A. C. Berg, Ssd: Single shot multibox detector, in: European conference on computer vision, Springer, 2016, pp. 21–37.

[35] J. Redmon, A. Farhadi, Yolo9000: Better, faster, stronger. arxiv, arXiv preprint arXiv:1612.08242 (2016).

[36] A. Farhadi, J. Redmon, Yolov3: An incremental improvement, Computer Vision and Pattern Recognition, cite as (2018).

[37] A. Bochkovskiy, C.-Y. Wang, H.-Y. M. Liao, Yolov4: Optimal speed and accuracy of object detection, arXiv preprint arXiv:2004.10934 (2020).

[38] T.-Y. Lin, P. Goyal, R. Girshick, K. He, P. Dollár, Focal loss for dense object detection, in: Proceedings of the IEEE international conference on computer vision, 2017, pp. 2980–2988.

[39] H. Law, J. Deng, Cornernet: Detecting objects as paired keypoints, in: Proceedings of the European Conference on Computer Vision (ECCV), 2018, pp. 734–750.

[40] Z. Yang, S. Liu, H. Hu, L. Wang, S. Lin, Reppoints: Point set representation for object detection, in: Proceedings of the IEEE International Conference on Computer Vision, 2019, pp. 9657–9666.

[41] Z. Tian, C. Shen, H. Chen, T. He, Fcos: Fully convolutional one-stage object detection, in: Proceedings of the IEEE international conference on computer vision, 2019, pp. 9627–9636.

[42] L. Tychsen-Smith, L. Petersson, Denet: Scalable real-time object detection with directed sparse sampling, in: Proceedings of the IEEE international conference on computer vision, 2017, pp. 428–436.

[43] Q. Wang, F. Qi, M. Sun, J. Qu, J. Xue, Identification of tomato disease types and detection of infected areas based on deep convolutional neural networks and object detection techniques, Computational Intelligence and Neuroscience 2019 (2019).

[44] S.-e.-A. Raza, G. Prince, J. P. Clarkson, N. M. Rajpoot, Automatic detection of diseased tomato plants using thermal and stereo visible light images, PloS one 10 (4) (2015) e0123262.

[45] H. Xu, Y. Ying, X. Fu, S. Zhu, Near-infrared spectroscopy in detecting leaf miner damage on tomato leaf, Biosystems Engineering 96 (4) (2007) 447–454.

[46] D. Kosmopoulos, C. Constantinopoulos, D. Papadimitriou, T. Manios, J. Fasoulas, M. Sfakiotakis, C. Stantoumis, I. Kalisperakis, A. Tsalavoutas, D. L., The soup project: current state and future activities, Information, Intelligence, Systems and Applications 1 (1) (2020) 94–98.

[47] L. Mkonyi, D. Rubanga, M. Richard, N. Zekeya, S. Sawahiko, B. Maiseli, D. Machuve, Early identification of tuta absoluta in tomato plants using deep learning, Scientific African 10 (2020) e00590.

[48] B. Espejo-Garcia, N. Mylonas, L. Athanasakos, S. Fountas, I. Vasilakoglou, Towards weeds identification assistance through transfer learning, Computers and Electronics in Agriculture 171 (2020) 105306.

[49] X. Chen, G. Zhou, A. Chen, J. Yi, W. Zhang, Y. Hu, Identification of tomato leaf diseases based on combination of abck-bwtr and b-arnet, Computers and Electronics in Agriculture 178 (2020) 105730.

[50] M. Arsenovic, M. Karanovic, S. Sladojevic, A. Anderla, D. Stefanovic, Solving current limitations of deep learning based approaches for plant disease detection, Symmetry 11 (7) (2019) 939.

[51] D. Hughes, M. Salathé, et al., An open access repository of images on plant health to enable the development of mobile disease diagnostics, arXiv preprint arXiv:1511.08060 (2015).

[52] A. Fuentes, S. Yoon, S. Kim, D. Park, A robust deep-learning-based detector for real-time tomato plant diseases and pests recognition, Sensors 17 (9) (2017) 2022.

[53] K. He, G. Gkioxari, P. Dollár, R. Girshick, Mask r-cnn, in: Proceedings of the IEEE international conference on computer vision, 2017, pp. 2961–2969.

[54] H. Xu, S. Zhu, Y. Ying, H. Jiang, Early detection of plant disease using infrared thermal imaging, in: Optics for Natural Resources, Agriculture, and Foods, Vol. 6381, International Society for Optics and Photonics, 2006, p. 638110.

[55] V. Bischoff, K. Farias, J. P. Menzen, G. Pessin, Technological support for detection and prediction of plant diseases: A systematic mapping study, Computers and Electronics in Agriculture 181 (2021) 105922.

[56] A. Kamilaris, F. X. Prenafeta-Boldú, Deep learning in agriculture: A survey, Computers and electronics in agriculture 147 (2018) 70–90.

[57] M. O. Lawal, Tomato detection based on modified yolov3 framework, Scientific Reports 11 (1) (2021) 1–11.

[58] N. Schor, A. Bechar, T. Ignat, A. Dombrovsky, Y. Elad, S. Berman, Robotic disease detection in greenhouses: Combined detection of powdery mildew and tomato spotted wilt virus, IEEE robotics and automation letters 1 (1) (2016) 354–360.

[59] X. Wang, J. Liu, Diseases detection of occlusion and overlapping tomato leaves based on deep learning 1, Frontiers in plant science (2021) 2812.

[60] J. Liu, X. Wang, Tomato diseases and pests detection based on improved yolo v3 convolutional neural network, Frontiers in plant science 11 (2020) 898.

[61] C. I. Fernández, B. Leblon, J. Wang, A. Haddadi, K. Wang, Detecting infected cucumber plants with close-range multispectral imagery, Remote Sensing 13 (15) (2021) 2948.

[62] Y. Xie, D. Plett, H. Liu, The promise of hyperspectral imaging for the early detection of crown rot in wheat, AgriEngineering 3 (4) (2021) 924–941.

[63] A. Benfenati, P. Causin, R. Oberti, G. Stefanello, Unsupervised deep learning techniques for powdery mildew recognition based on multispectral imaging, arXiv preprint arXiv:2112.11242 (2021).

[64] Y. Peng, M. Dallas, J. T. Ascencio-Ibáñez, S. Hoyer, J. Legg, L. Hanley-Bowdoin, B. Grieve, H. Yin, Early detection of plant virus infection using multispectral imaging and spatial-spectral machine learning (2021).

[65] P. Karpyshev, V. Ilin, I. Kalinov, A. Petrovsky, D. Tsetserukou, Autonomous mobile robot for apple plant disease detection based on cnn and multi-spectral vision system, in: 2021 IEEE/SICE International Symposium on System Integration (SII), IEEE, 2021, pp. 157–162.

[66] S. U. Rasheed, W. Muhammad, I. Qaiser, M. J. Irshad, A multispectral pest-detection algorithm for precision agriculture, Engineering Proceedings 12 (1) (2021) 46.

[67] I. H. Khan, H. Liu, W. Li, A. Cao, X. Wang, H. Liu, T. Cheng, Y. Tian, Y. Zhu, W. Cao, et al., Early detection of powdery mildew disease and accurate quantification of its severity using hyperspectral images in wheat, Remote Sensing 13 (18) (2021) 3612.

[68] P. Wspanialy, M. Moussa, Early powdery mildew detection system for application in greenhouse automation, Computers and Electronics in Agriculture 127 (2016) 487–494.

[69] K. Kamal, Z. Yin, M. Wu, Z. Wu, Depthwise separable convolution architectures for plant disease classification, Computers and Electronics in Agriculture 165 (2019) 104948.

[70] D. Argüeso, A. Picon, U. Irusta, A. Medela, M. G. San-Emeterio, A. Bereciartua, A. Alvarez-Gila, Few-shot learning approach for plant disease classification using images taken in the field, Computers and Electronics in Agriculture 175 (2020) 105542.

[71] A. K. Rangarajan, R. Purushothaman, A. Ramesh, Tomato crop disease classification using pre-trained deep learning algorithm, Procedia Computer Science 133 (2018) 1040 – 1047, international Conference on Robotics and Smart Manufacturing (RoSMa2018).

[72] J. G. A. Barbedo, Plant disease identification from individual lesions and spots using deep learning, Biosystems Engineering 180 (2019) 96–107.

[73] M. M. Ozguven, K. Adem, Automatic detection and classification of leaf spot disease in sugar beet using deep learning algorithms, Physica A: Statistical Mechanics and its Applications 535 (2019) 122537.

[74] J. Chen, J. Chen, D. Zhang, Y. Sun, Y. A. Nanehkaran, Using deep transfer learning for image-based plant disease identification, Computers and Electronics in Agriculture 173 (2020) 105393.

[75] Y. Elad, Y. Messika, M. Brand, D. R. David, A. Sztejnberg, Effect of colored shade nets on pepper powdery mildew (leveillula taurica), Phytoparasitica 35 (3) (2007) 285–299.

[76] D. Savvas, K. Adamidis, Automated management of nutrient solutions based on target electrical conductivity, ph, and nutrient concentration ratios, Journal of Plant Nutrition 22 (9) (1999) 1415–1432. arXiv:https://doi.org/10.1080/01904169909365723, doi:10.1080/01904169909365723.
URL https://doi.org/10.1080/01904169909365723

[77] C. Balas, V. Papadakis, N. Papadakis, A. Papadakis, E. Vazgiouraki, G. Themelis, A novel hyper-spectral imaging apparatus for the non-destructive analysis of objects of artistic and historic value, Journal of Cultural Heritage 4 (2003) 330–337.

[78] C. Balas, C. Pappas, G. Epitropou, Multi/hyper-spectral imaging, in: Handbook of biomedical Optics, CRC Press, 2016, pp. 151–184.

[79] C. Balas, G. Epitropou, A. Tsapras, N. Hadjinicolaou, Hyperspectral imaging and spectral classification for pigment identification and mapping in paintings by el greco and his workshop, Multimedia Tools and Applications 77 (8) (2018) 9737–9751.

[80] A. Dutta, A. Zisserman, The via annotation software for images, audio and video, in: Proceedings of the 27th ACM international conference on multimedia, 2019, pp. 2276–2279.

[81] M. A. Hassan, M. Yang, A. Rasheed, G. Yang, M. Reynolds, X. Xia, Y. Xiao, Z. He, A rapid monitoring of ndvi across the wheat growth

cycle for grain yield prediction using a multi-spectral uav platform, Plant science 282 (2019) 95–103.

[82] N. Pettorelli, J. O. Vik, A. Mysterud, J.-M. Gaillard, C. J. Tucker, N. C. Stenseth, Using the satellite-derived ndvi to assess ecological responses to environmental change, Trends in ecology & evolution 20 (9) (2005) 503–510.

[83] J. A. Gamon, C. B. Field, M. L. Goulden, K. L. Griffin, A. E. Hartley, G. Joel, J. Penuelas, R. Valentini, Relationships between ndvi, canopy structure, and photosynthesis in three californian vegetation types, Ecological Applications 5 (1) (1995) 28–41.

[84] D. Grados, X. Reynarfaje, E. Schrevens, A methodological approach to assess canopy ndvi–based tomato dynamics under irrigation treatments, Agricultural Water Management 240 (2020) 106208.

[85] D. Garcia-Garcia, X. R. la Rosa, D. G. Bedoya, E. Schrevens, Linear mixed model analysis of ndvi-based canopy coverage, extracted from sequential uav multispectral imagery of an open field tomato irrigation experiment, Computers and Electronics in Agriculture 189 (2021) 106399.

[86] R. Fortes, M. H. Prieto, J. M. Terrón, J. Blanco, S. Millan, C. Campillo, Using apparent electric conductivity and ndvi measurements for yield estimation of processing tomato crop, Transactions of the ASABE 57 (3) (2014) 827–835.

[87] M. Mastrorilli, P. Campi, D. Palumbo, F. Modugno, Ground-based remote sensing for assessing tomato water-status, Italian Journal of Agronomy 5 (2) (2010) 177–184.

[88] F. Padilla, M. Peña-Fleitas, M. Gallardo, R. Thompson, Threshold values of canopy reflectance indices and chlorophyll meter readings for optimal nitrogen nutrition of tomato, Annals of Applied Biology 166 (2) (2015) 271–285.

[89] L. Ding, Y. Wang, R. Laganière, D. Huang, X. Luo, H. Zhang, A robust and fast multispectral pedestrian detection deep network, Knowledge-Based Systems 227 (2021) 106990.

[90] T.-Y. Lin, M. Maire, S. Belongie, J. Hays, P. Perona, D. Ramanan, P. Dollár, C. L. Zitnick, Microsoft coco: Common objects in context, in: European conference on computer vision, Springer, 2014, pp. 740–755.

[91] J. Deng, W. Dong, R. Socher, L.-J. Li, K. Li, L. Fei-Fei, ImageNet: A large-scale hierarchical image database, in: 2009 IEEE conference on computer vision and pattern recognition, Ieee, 2009, pp. 248–255.